A New Compact Soft Open Point Based on Cascaded H-Bridge and Mixed-Frequency Modulation

Haixi Zhao, Wu Chen, *Senior Member, IEEE*, Jianxi Lan, Yubo Yuan, and Yeyuan Xie

***Abstract*—As a power electronic device in place of normal open point, the soft open point (SOP) can improve the operating flexibility of a distribution network. Most of the existing SOP projects adopt the back-to-back modular multilevel converter (BTB-MMC) topology. However, the BTB-MMC requires a large number of submodules, which is costly and bulky. In this article, a mixed-frequency modulation based SOP (MFSOP) topology is proposed. The proposed MFSOP consists of a shunt cascaded H-bridge (CHBs), multiple series CHBs, and multiple *LC* resonance branches. Each terminal is equipped with a Y-△ transformer to isolate the medium-frequency zero sequence voltage introduced by the mixed-frequency modulation from the power grid. Compared with the traditional BTB-MMC, the proposed MFSOP can reduce the number of submodules, which makes the SOP more compact in size. The circulating current models are derived, and two circulating current suppression strategies are proposed based on circulating current models. Then, the control strategies are described and the key parameters are designed. Finally, the correctness and validity of the proposed MFSOP are verified by simulation and experimental results.**

***Index Terms*—Circulating current model, distribution network, mixed-frequency modulation, soft open point.**

I. INTRODUCTION

WITH the development of distributed energy resources (DERs) and loads, such as photovoltaic plants, wind turbines, and electric vehicles, the operation of distribution network (DN) is getting more and more complex. Higher peak demand, higher voltage fluctuation, and higher voltage drop on feeder makes the traditional DN suffer a serious safely and stability operational problems due to the great uncertainties in local power generation and consumption [1].

To host the increasing power demand and generation, one effective way is to upgrade and reconfigure the existing radially operated DN to a meshed DN [2], [3]. However, traditional meshed DN needs sophisticated and costly protection arrangement to function [4]. Another way is to add reactive power compensation devices, such as switched capacitor banks (CBs) or on-load tap changer (OLTC) [5], [6], to improve the operational safely and reliability of DN. However, low response of these traditional equipment makes it not suitable for the DN of high penetration DERs.

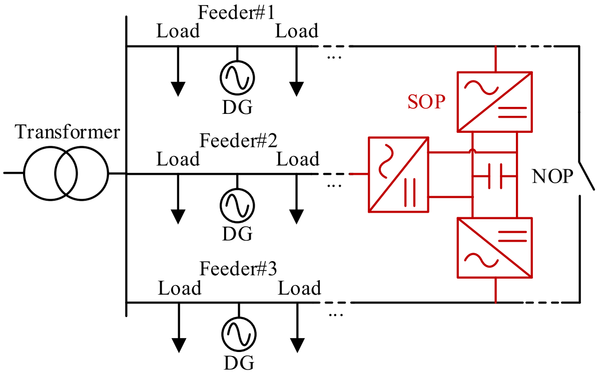

Fig. 1. Basic architecture of the multiport SOP in DNs.

In order to solve the above problems, soft open point (SOP) is proposed [7], [8]. The SOP, as an emerging power electronic device in DN, is usually placed normally open points (NOP) to provide flexible and accurate power and voltage control [1], while under faulty conditions, the SOP can quickly isolate faults and provide effective voltage support [9], [10], [11]. It not only gives the advantage of both radial DN having simple protection system and meshed DN with higher reliability [4], but also has fast response of power electronic converter. As shown in Fig. 1, the SOP is typically used to connect two or more three-phase feeder branch ends that are connected to the same substation to construct a ring-type net, so they have the same frequency, usually the same nominal voltage and a small phase shift.

Many researchers have proposed different SOP topologies. In general, the topologies of SOP are classified into three categories: series-type SOP [12], [13], [14], shunt-type SOP [15], [16], [17], and series-shunt-type SOP [18], [19], [20], [21].

The series-type SOP, such as static synchronous series compensators (SSSC) [12], is connected in series on two feeders to control the voltage across the transmission line and is subjected to the voltage difference between the two ac feeders. However, it requires the orthogonality of their terminal voltage and current to maintain the voltage balance of submodule capacitors, which restricts the power flow regulation capability of the SSSC.

Received 31 May 2024; revised 29 September 2024; accepted 18 November 2024. Date of publication 28 November 2024; date of current version 26 December 2024. This work was supported by the National Key Research and Development Program of China under Grant 2023YFB2407403. Recommended for publication by Associate Editor F. Dijkhuizen. *(Corresponding author: Wu Chen.)*

Haixi Zhao, Wu Chen, and Jianxi Lan are with the Center for Advanced Power Conversion Technology and Equipment, School of Electrical Engineering, Southeast University, Nanjing 210096, China (e-mail: 230218870@seu.edu.cn; chenwu@seu.edu.cn; jxlan@seu.edu.cn).

Yubo Yuan is with the State Grid Jiangsu Electric Power Company, Ltd., Research Institute, Nanjing 210096, China (e-mail: yuanyubo@js.sgcc.com.cn).

Yeyuan Xie is with the NR Electric Company, Ltd., Nanjing 210096, China (e-mail: xieyy@nrec.com).

Color versions of one or more figures in this article are available at https://doi.org/10.1109/TPEL.2024.3507914.

Digital Object Identifier 10.1109/TPEL.2024.3507914

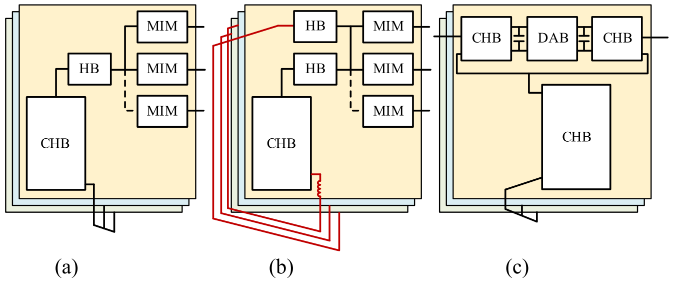

Fig. 2. State of arts series-shunt type SOPs. (a) [18]. (b) [19]. (c) [20].

Another series-type SOP, the direct MMC (DMMC) is proposed in [13]. The DMMC topology is more compact in size than back-to-back modular multilevel converter (BTB-MMC) because it only requires the half number of capacitors and inductors. However, the coupling of currents between the two feeders entails a coupled reactive power, which means the converter inject or consume exactly the same amount of reactive power in both feeders [14]. This feature limits the reactive power compensation capacity of DMMC.

The shunt-type SOP topologies can be divided into two converters: both the two converters are subjected to the voltage of power grids, respectively. The shunt-type SOPs are the most popular SOP topologies in industry, such as BTB two-level voltage source converter for low voltage and BTB-MMC [15] for medium or high voltage power grids. In addition to BTB-MMC, power electronic transformer (PET) can also be used as shunt-type SOP in medium voltage DN, such as two terminal SOP topology with two cascaded H-bridges (CHBs) and one cascaded dual active bridge converter [16], multiterminal SOP topology with multiple CHBs and one multiactive bridge converter [17]. These topologies have more power flow regulation capability. Furthermore, the lightweight topology based on multiplexing arm MMC [22], [23], [24] can significantly reduce the number of submodules and improve their power density. Evidently, it cannot be overlooked that a large number of capacitors and semiconductors are still employed compared to the series-type SOP.

In recent years, a lot of series-shunt-type SOP topologies are proposed. The series converter is subjected to the voltage difference between the two ac feeders and the shunt converter is subjected to the voltage of the power grid. The series-shunt-type SOP have large operation range comparing to series-type SOP and more compact in size and high efficiency comparing to shunt-type SOP. As shown in Fig. 2, in [18], the series-shunt multiport SOP (S^2-SOP) is proposed to reduce the number of active and passive components by multiplexing the CHB modules. The interconnection module (half bridge module) is adopted to interconnect different feeders. However, the energy balance ability of the S^2-SOP is constrained by shunt current in reactive power compensation mode, which limits its operating range [19]. To overcome this drawback, the delta-type series-shunt multiport SOP (D-S^3NOP) is proposed in [19]. By adopting delta-type CHB configuration, an additional degree of freedom and energy path are constructed to achieve energy balance. Although the D-S^3NOP expanding the power flow regulation range, both S^2-SOP and D-S^3NOP do not have fault isolation capability. By replacing the single half-bridge in the interconnection module with CHB, the shared modular SOP (SMSOP) is proposed in [20]. More complex module interconnection gives it larger operation range and fault isolation can be achieved. However, it is not suitable for operation in small phase shift between the two feeders. In [21], a distributed power flow controller (DPFC) is proposed. The DPFC, as a new PFC topology adopting mixing frequency modulation method, has each H-bridge cells connected to the grid through the transformer. When a fault occurs, the DPFC is bypassed and cannot isolate the fault current.

Compared with the previous work on the SOP, this article proposes a new mixed-frequency modulation based SOP topology (MFSOP), which can save the quantity of submodules and reduce loss. In addition, the operation principles are illustrated and the circulating current models are derived. The mixed-frequency modulation introduces a medium-frequency circulating current into the device, which increases the current stress. Therefore, two circulating current suppression methods are proposed. A parameter design method suitable for mixed-frequency modulation converter is derived and an example is given. In addition, the comparison of the MFSOP and other SOP topologies is listed.

The rest of this article is organized as follows. Section II describes the topology structure and operation principle of MFSOP. The circulating current model is derived in detail in unity power factor and reactive power compensation mode in Section III. In Section IV, two circulating current suppression strategies are proposed to reduce the current stress. In Section V presents the control strategies of MFSOP, including the series CHB and the shunt CHB control strategies. Key parameters are designed and comparison with other topologies are carried in Section VI. Simulation and experiment results are presented in Section VII. Finally, Section VIII concludes this article.

II. PROPOSED MFSOP

A. *Basic Idea and the Derivation of the Proposed MFSOP*

In Fig. 3(a), a CHB is connected in series between two feeders. If the terminal voltage and current of the series CHB are not orthogonal, the line-frequency voltage and current will charge or discharge the submodule capacitors, which results in unbalanced submodule capacitor dc voltage.

According to the orthogonality of trigonometric functions, the average power of the voltages and currents of different frequencies over a common period is zero. Therefore, it is possible to inject a medium-frequency component into the line-frequency modulation wave, meaning the modulation wave contains both line-frequency and medium-frequency components. The power, which line-frequency voltage multiplied by line-frequency current (red) and medium-frequency voltage multiplied by medium-frequency current (blue) is shown in Fig. 3(b). The two power have the same average value but opposite sign, which means the total average power of submodule capacitor is zero. And the energy of submodule capacitor is balanced, as shown in Fig. 3(c) [25].

Therefore, from a power perspective, the two frequency components are decoupled from each other and can be used to control

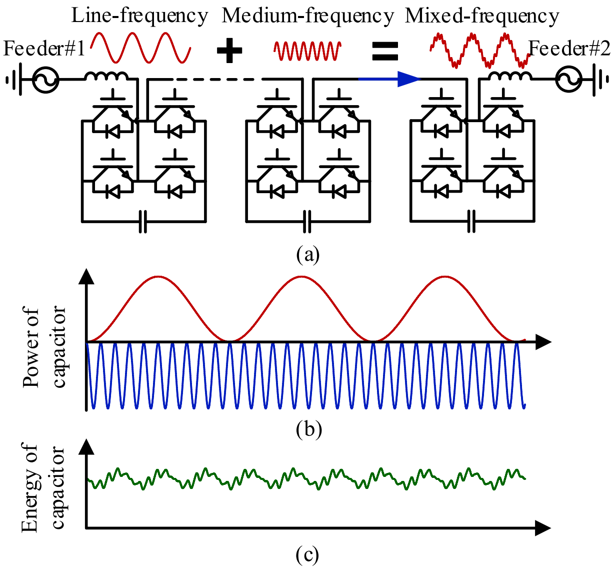

Fig. 3. Waveforms of mixed-frequency modulation. (a) Series CHB topology. (b) Power of line-frequency components (red) and medium-frequency components (blue). (c) Energy of capacitor.

two independent targets separately. Based on this principle, the MFSOP topology is proposed in this article.

B. Topology of MFSOP

Fig. 4 shows the topology of the proposed MFSOP. The topology consists of three parts: one shunt CHB, i.e., CHB$_1$, $(n-1)$ series CHB and $(n-1)$ resonance branches. The shunt CHB connected in parallel on feeder#1, while the series CHB$_i$ $(i = 2 \sim n)$ are connected in series between feeder#1 and feeder#*i*. The resonant branch, which adopts series resonant *LC* in here, connected in parallel on the corresponding feeder#*i* to provide a path for the medium-frequency circulating current. In order to prevent the medium-frequency current flowing into the power grid and causing harmonic pollution, the three-phase waveforms of the medium-frequency component are the same, i.e., the zero-sequence component is used, and Y-△ transformers are equipped at each ac port to isolate the medium-frequency zero-sequence component from the power grid. It is worth noting that power transformers have been widely equipped in the traditional BTB-MMC to isolate grid fault in most scenarios.

In light of the circuit superposition theorem, Fig. 5 shows current paths of line-frequency and medium-frequency. In Fig. 5(a), the line-frequency current flows through series CHB and shunt CHB but is blocked by the resonant branch. In Fig. 5(b), the medium-frequency current flows through series CHB, shunt CHB and resonant branch, but it is blocked by the power transformer.

When the line-frequency current flows through the series CHB, if the terminal voltage of the series CHB is not orthogonal to the current, the line-frequency current will charge or discharge its submodule dc capacitors, and the dc voltage cannot be maintained balance. By injecting the medium-frequency current, a circulating current path is formed by the "shunt CHB - series CHB - resonant LC", as shown in Fig. 5(b). The medium-frequency circulating current discharges or charges the submodule capacitor to maintain the equilibrium of the series CHB module voltage. The specific process is as follows.

As shown in Fig. 6, when the line-frequency current charges the submodule capacitors of the series CHB, the voltage of dc capacitor rises. Therefore, the medium-frequency circulating current needs to discharge the submodule capacitor of series CHB, transferring capacitor energy from series CHB to the shunt CHB module capacitor, and then the line-frequency current of shunt CHB releases the energy back to the grid. Similarly, when the line-frequency current discharges module capacitor of the series CHB, the voltage of dc capacitor drops. Therefore, the medium-frequency circulating current needs to charge the submodule capacitor of series CHB, and the charging energy comes from module capacitor of the shunt CHB. In order to ensure the voltage equilibrium of the shunt CHB module capacitor, the shunt CHB will absorb energy from the grid through the line-frequency current. In steady-state, the charging and discharging power of the line-frequency current to the series CHB module capacitor is exactly equal to the discharging and charging power of the medium-frequency circulating current, which together maintain the module capacitor voltage balance.

Since there are both line-frequency and medium-frequency currents existence in the MFSOP, the medium-frequency circulating current of the MFSOP needs to be analyzed in following section.

III. CIRCULATING CURRENT MODEL

The mixed-frequency modulation method injects two frequency currents into the circuit. In this section, the MFSOP circulating current is modeled in unity power factor mode and reactive power compensation mode, respectively.

A. Circulating Current Model in Unity Power Factor Mode

According to the operation principle of the MFSOP in Section II, the vector diagram of line-frequency voltage and current is analyzed to illustrate the circulating current of the proposed MFSOP topology, as shown in Fig. 7. For simplicity, it is assumed that the MFSOP operates in unity power factor mode.

Assuming that the current flows into the grid from the device is positive reference direction, as shown in Fig. 4. The amplitude U_{gi} of grid voltage u_{gi} $(i = 1, 2,\ldots, n)$ on each ac feeder is the same, i.e., $U_{gi} = U_g$. The series CHB$_i$ is subjected to the voltages difference $u_{\mathrm{CHB}\,i}$ between the two feeders, which the amplitude of $u_{\mathrm{CHB}\,i}$ is approximated by

$$U_{\mathrm{CHB}i} = 2U_g \sin\frac{\theta_i + \gamma_i - \gamma_1}{2} \tag{1}$$

where θ_i is the phase shift between the voltages of the two feeders interconnected by CHB$_i$. γ_i is the phase shift caused by the filter inductance L_i at the port of the *i*th ac feeder, $\gamma_i = \arctan(\omega L_i P_i/3{U_g}^2)$. P_i is the *i*th ac feeder active power, and ω is line angular frequency.

It is worth noting that $u_{\mathrm{CHB}\,i}$ is perpendicular to the angle bisector of $\angle u_i$-u_1. Therefore, the phase of $u_{\mathrm{CHB}\,i}$ is

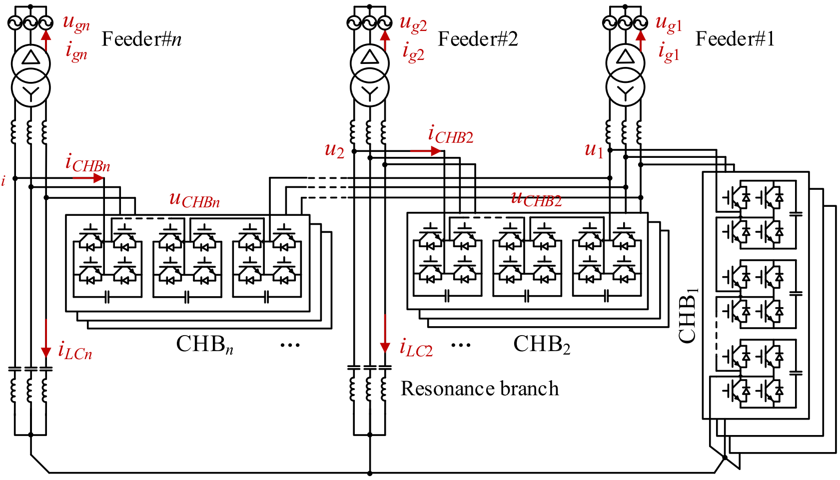

Fig. 4. Topology of MFSOP.

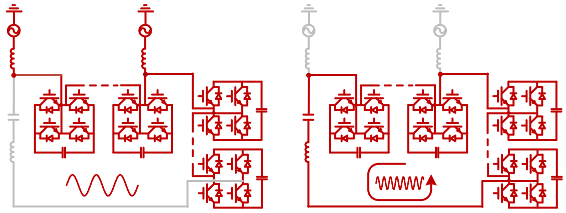

(a) (b)

Fig. 5. Current paths. (a) Line-frequency current. (b) Medium-frequency current.

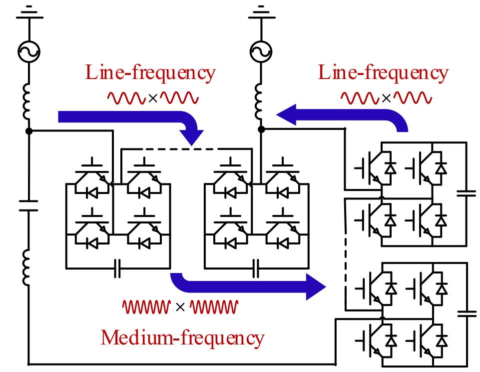

Fig. 6. Power flow path.

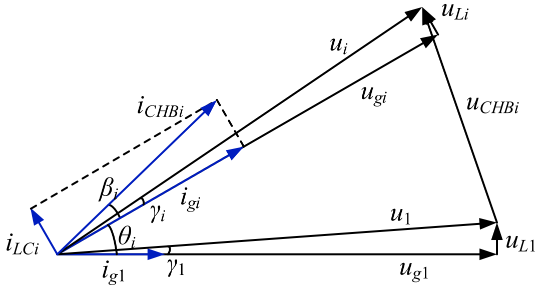

Fig. 7. Phase diagram of MFSOP in unity power factor mode.

calculated as

$$\angle u_{\mathrm{CHB}i} = 90^\circ + \frac{\theta_i + \gamma_1 + \gamma_i}{2}. \tag{2}$$

The line-frequency current $i_{\mathrm{CHB}i}$ flowing through the series CHB$_i$ is

$$I_{\mathrm{CHB}i} = \frac{\sqrt{\left(3\omega C_{ri} U_g^2\right)^2 + P_i^2}}{3U_g}. \tag{3}$$

And the phase of $i_{\mathrm{CHB}i}$ is

$$\begin{aligned} \angle i_{\mathrm{CHB}i} &= \theta_i + \mathrm{atan}\left(\frac{3\omega C_{ri} U_g^2}{P_i}\right) \\ &= \begin{cases} \theta_i + \beta_i, & P_i > 0 \\ \theta_i + \beta_i + 180^\circ, & P_i < 0 \end{cases} \end{aligned} \tag{4}$$

where C_{ri} is the resonant capacitor connected in parallel to the ith feeder. The symbolic, atan(.), is four-quadrant inverse tangent function, i.e., $\beta_i = \arctan(3\omega C_{ri} {U_g}^2 / P_i)$. The positive reference direction of active power P_i is defined as the flow of power from the device to the power grid.

According to (2) and (4), the phase difference α_i of the terminal voltage and current of series CHB$_i$ are as follows:

$$\alpha_i = \angle u_{\mathrm{CHB}i} - \angle i_{\mathrm{CHB}i} = \pm 90^\circ + \frac{-\theta_i + \gamma_i + \gamma_1}{2} - \beta_i. \tag{5}$$

Therefore, according to (1), (3), and (5), the active power absorbed by series CHB$_i$ is

$$\begin{aligned} P_{\mathrm{CHB}i} &= 3U_{\mathrm{CHB}i} I_{\mathrm{CHB}i} \cos\alpha_i \\ &= \pm 2\sqrt{\left(3\omega C_{ri} U_g^2\right)^2 + P_i^2} \sin\frac{\theta_i + \gamma_i - \gamma_1}{2} \\ &\times \sin\left(\frac{\theta_i - \gamma_i - \gamma_1}{2} + \beta_i\right) \end{aligned} \tag{6}$$

which is “+” if $P_i > 0$ and “–” if $P_i < 0$.

In order to maintain the module capacitor voltage of series CHB$_i$ balance, it is necessary to ensure that the power $P_{\mathrm{MF}i}$

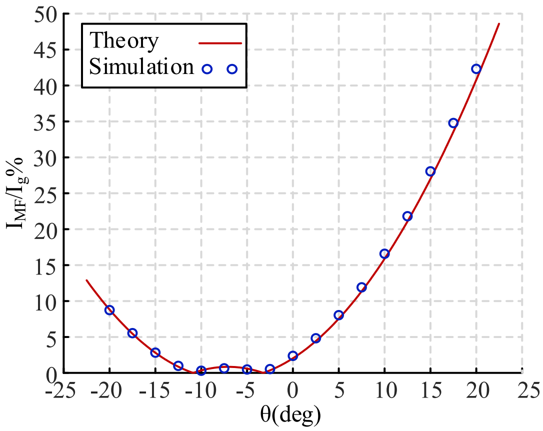

Fig. 8. Simulation and theoretical results of the medium-frequency circulating current under different power and phase shift condition.

TABLE I
SIMULATION PARAMETERS

Parameter	Value
Voltage of feeder#1	10 kV
Voltage of feeder#2	10 kV
Medium-frequency voltage	1.2 kV
Rated power	3 MW
Filter inductor	4 mH
Resonant inductor	10 mH
Resonant capacitor	10 μF

of the medium-frequency voltage $u_{\mathrm{MF}\,i}$ and current $i_{\mathrm{MF}\,i}$ for charging the module capacitor is equal to the line-frequency power $P_{\mathrm{CHB}\,i}$ discharging the module capacitor. The medium-frequency voltage and current are in phase to maximize the charging or discharging capabilities of the submodule dc capacitor. Namely

$$P_{\mathrm{CHB}i} = P_{\mathrm{MF}i} = 3U_{\mathrm{MF}i} I_{\mathrm{MF}i}. \tag{7}$$

Thus, the medium-frequency circulating current can be obtained as

$$I_{\mathrm{MF}i} = \pm\frac{2\sqrt{\left(3\omega C_{ri}U_g^2\right)^2 + P_i^2}}{3U_{\mathrm{MF}i}} \sin\frac{\theta_i+\gamma_i-\gamma_1}{2} \times \sin\left(\frac{\theta_i-\gamma_i-\gamma_1}{2}+\beta_i\right). \tag{8}$$

Fig. 8 shows the simulation results and theoretical results of the medium-frequency circulating current under different active power and phase shift condition. The circuit parameters are shown in Table I. In Fig. 8, the horizontal axis represents the phase shift between the two feeders and the vertical axis represents the ratio of medium-frequency circulating current to line-frequency current. It can be seen that the larger phase shift leads to the larger circulating current. The theoretical results coincide with the simulated results, which verifies the correctness of the theoretical analysis in this section.

It is worth noting that the magnitude of the circulating current is not symmetrical about the 0°-axis, which is due to the fact that a certain amount of line-frequency current flows through the *LC* branch, resulting in a phase shift of $i_{\mathrm{CHB}\,i}$, which is reflected in term β_i of (8).

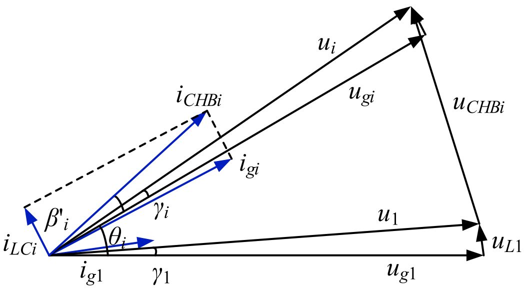

Fig. 9. Phase diagram of MFSOP in reactive power compensation mode.

B. Circulating Current Model in Reactive Power Compensation Mode

Since each ac feeder is connected by a CHB, the MFSOP can independently control the reactive power at each port. However, when MFSOP injects reactive power to the feeder, the phase of i_{gi} is shifted. The phase difference α_i between $u_{\mathrm{CHB}\,i}$ and $i_{\mathrm{CHB}\,i}$ is changed, which will change the circulating current. Therefore, the reactive power operating range of the MFSOP needs to be considered in here.

The steady-state phase diagram of the line-frequency voltage and current in reactive power compensation mode is shown in Fig. 9. The amplitude and phase of $u_{\mathrm{CHB}\,i}$ are the same as (1) and (2). However, due to the presence of reactive power, the amplitude and phase of $i_{\mathrm{CHB}\,i}$ change, and according to the cosine theorem in Fig. 9, the amplitude and phase of $i_{\mathrm{CHB}\,i}$ are, respectively, as follows:

$$I_{\mathrm{CHB}i} = \sqrt{\left(\omega C_r U_g\right)^2 + I_{gi}^2 \pm \frac{2}{3}\omega C_r S_i \sin\left(a\tan\frac{Q_i}{P_i}\right)} \tag{9}$$

$$\begin{aligned}\angle i_{\mathrm{CHB}i} &= \theta_i + \mathrm{a}\tan\left(\frac{3\omega C_{ri}U_g^2 + Q_i}{P_i}\right)\\ &= \begin{cases}\theta_i + \beta, & P_i > 0\\ \theta_i + \beta'_i + 180^\circ, & P_i < 0\end{cases}.\end{aligned} \tag{10}$$

Then, the circulating current of MFSOP can be written as

$$I_{\mathrm{MF}i} = \frac{2}{3U_{\mathrm{MF}}}\sqrt{\left(3\omega C_r U_g^2\right)^2 + S_i^2 \pm 6\omega C_r U_g^2 S_i \sin\left(a\tan\frac{Q_i}{P_i}\right)} \times \sin\frac{\theta_i+\gamma_i-\gamma_1}{2}\sin\left(\frac{\theta_i-\gamma_i-\gamma_1}{2}+\beta'_i\right) \tag{11}$$

where$\beta'_i = \arctan\frac{3\omega C_{ri}U_g^2+Q_i}{P_i}$, S_i is the apparent power.

Fig. 10 shows the simulation and theoretical results of the medium circulating current in reactive power compensation mode, and the circuit parameters are shown in Table I. The theoretical results almost coincide with the simulation results, which verifies the correctness of the theoretical analysis in this section.

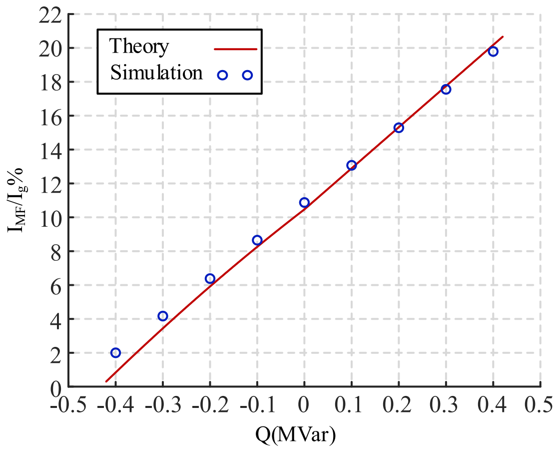

Fig. 10. Simulation and theoretical results of the medium-frequency circulating current in reactive power compensation mode.

TABLE II
RELATIONSHIP BETWEEN CIRCULATING CURRENT AND REACTIVE POWER

power flow direction	Absorption of inductive reactive power	Absorption of capacitive reactive power
feeder→MFSOP	circulating current increases	circulating current decreases
MFSOP→feeder	circulating current decreases	circulating current increases

It can be seen from Fig. 10 that the reactive power can increase or decrease the amplitude of circulating current. Therefore, in the early stage of the SOP project, the phase shift and the requirement of reactive power compensation should be investigated in advance to ensure that the reactive power is able to reduce the amplitude of circulating current.

IV. CIRCULATING CURRENT SUPPRESSION METHODS

The mixed-frequency modulation introduces circulating current into the MFSOP, resulting in a large current stress. In this section, two circulating current suppression methods are proposed to reduce current stress.

A. Changing the Power Factor

According to (11), when the power flows from MFSOP to feeder#*i*, a small amount of inductive reactive power absorbed by MFSOP can significantly reduce the circulating current, while a small amount of capacitive reactive power absorbed by MFSOP can significantly increase the circulating current; When the power flows from feeder#*i* to MFSOP, a small amount of capacitive reactive power absorbed by MFSOP can significantly reduce the circulating current, while a small amount of inductive reactive power absorbed by MFSOP can significantly increase the circulating current. Those relationships are listed in Table II.

Fig. 11 shows the phase diagram of MFSOP at different power factors. The MFSOP absorbs inductive reactive power in Fig. 11(a), which decreases the phase difference α_i between $u_{\mathrm{CHB}\,i}$ and $i_{\mathrm{CHB}\,i}$. As a result, the circulating current is larger than that of unity power factor mode in Fig. 11(b).

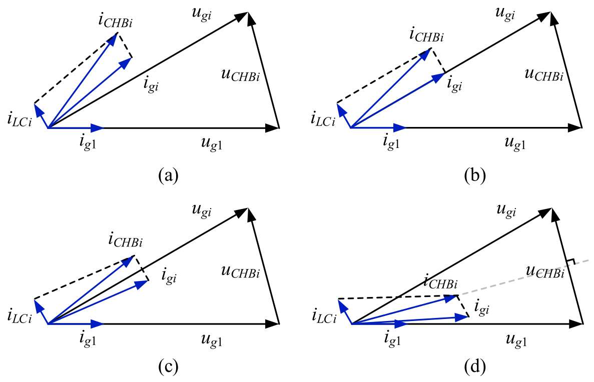

Fig. 11. Phase diagram of MFSOP at different power factor.

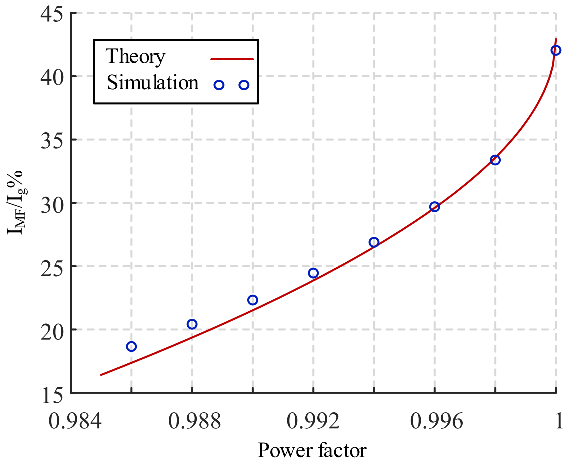

Fig. 12. Simulation and theoretical results of the medium-frequency circulating current at different power factor.

When the MFSOP absorbs capacitive reactive power, as shown in Fig. 11(c) and (d), the phase difference between $u_{\mathrm{CHB}\,i}$ and $i_{\mathrm{CHB}\,i}$ increases, and thus, the circulating current decreases. When the capacitive reactive power is absorbed so that $i_{\mathrm{CHB}\,i}$ is exactly perpendicular to $u_{\mathrm{CHB}\,i}$, as shown in Fig. 11(d), the submodule capacitor of series CHB will not charge or discharge, and the circulating current is zero at this time.

Fig. 12 shows the simulation and theoretical results of the medium circulating current at different power factor. The phase shift between the two feeders is set as 20°, and the circuit parameters are shown in Table I. When the MFSOP operates at unit power factor, the circulating current is almost 42% of the gird current, resulting in a high current stress. By slightly reducing the power factor from 1 to 0.987, the circulating current is effectively reduced to 20% of the grid current. Therefore, reducing the power factor can effectively suppress the circulating current.

B. Using Medium-Frequency Zero-Sequence Square Waves

According to (8), the circulating current can be suppressed effectively by means of increasing the medium-frequency voltage U_{MF}. However, a higher medium-frequency

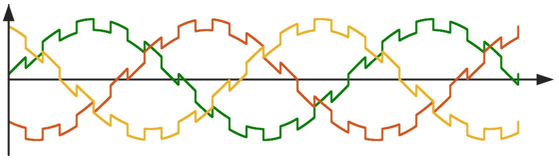

Fig. 13. Modulation waves of line-frequency component superposites medium-frequency zero sequency square wave component.

voltage U_{MF} leads to more submodules, which increases the cost.

Since the resonant *LC* branch is similar to a band-pass filter, the medium-frequency voltage can be the square wave instead of the sinusoidal wave, as shown in Fig. 13. This approach is based on the fact that a sinusoidal wave can be obtained by band-pass filtering a square wave, and the amplitude is $4/\pi$ times than that of the square wave, which means the circulating current is reduced by 21.5%.

V. Control Strategy of MFSOP

The proposed MFSOP control strategy is shown in Fig. 14. The control strategies include shunt CHB control strategy and series CHB control strategy, where the series CHB control strategies include line-frequency control strategy and medium-frequency control strategy.

A. *Control Strategy of Shunt CHB*

Fig. 14(a) shows the phase locked loop, coordinate transformation and power calculation for the shunt CHB and each series CHB.

Fig. 14(b) shows the shunt CHB control strategy. The control strategy is similar to that of the conventional STATCOM [26]. The grid current of feeder#1 is regulated by current inner loop controller. The submodule capacitor voltage is regulated by dc voltage outer loop controller to generate d-axis current reference $i_{gd1}{}^{*}$, and a power controller generates *q*-axis current reference $i_{gq1}{}^{*}$ to regulate reactive power of feeder#1. u_{bala1}, u_{balb1}, and u_{balc1} are added to modulation waves to realize the clustered and individual voltage balancing, and the specific voltage balancing control has been well investigated [27], and will not be repeated in this article. The medium-frequency zero-sequence voltage $u_{\mathrm{MF}\,abc1}$ are superimposed at the modulation waves. It is worth noting that $u_{\mathrm{MF}\,abc1} = U_{\mathrm{MF}}\cos(\theta_{\mathrm{MF}})$, which is synthesized directly by the constant U_{MF} and the integral of constant ω_{MF}.

B. *Control Strategy of Series CHB*

The control strategies of the series CHB are divided into two parts: 1) the line-frequency control strategy and 2) the medium-frequency control strategy.

The line-frequency control strategy of series CHB is shown in Fig. 14(c). The grid current of feeder#*i* is regulated by current inner loop controller and the active and reactive power of feeder#*i* is regulated by power outer loop controller to generate the current reference $i_{di}{}^{*}$ and $i_{qi}{}^{*}$. The u_{balai}, u_{balbi}, and u_{balci}, which is generated by the clustered voltage balancing controller, is responsible for balancing the clustered dc voltage of phase A, B, and C.

The medium-frequency circulating currents of phase A, B, and C are controlled independently. In Fig. 14(d), the medium-frequency control strategy of phase A is presented. The control strategy is similar to traditional single phase two-level full-bridge inverter. Each submodule of the phase A has its own controller. The outer loop controller regulates submodule dc voltage: the average dc voltage of phase A as reference to generate the amplitude reference $I_{\mathrm{MF}}{}^{*}$ of circulating current $i_{\mathrm{MF}}{}^{*}$ though PI controller. The phase θ_{MF} of $i_{\mathrm{MF}}{}^{*}$ is the same with the phase of u_{MF1} in Fig. 14(b). The medium-frequency circulating current is regulated by PR controller of inner control loop, and a medium-frequency voltage feedforward is added to the output of PR controller.

VI. Design and Comparisons

Due to the mixed-frequency modulation, the design method of submodule capacitor is different from that of traditional SOP. Thus, some key parameters, including *LC* branch, submodule capacitor and number of submodule, are designed in this section. An example is given, and the comparison of the MFSOP and other SOP topologies is listed.

A. *Key Parameters Design*

1) Resonance Parameters Design: According to (8), the relationship between resonant capacitor and circulating current can be obtained, as shown in Fig. 15. It can be seen that a larger resonant capacitor will increase the circulating current, which leads to a larger current stress. Thus, the current stress determines the maximum $\mathrm{C}_{r\max}$ of the resonant capacitor.

Define the ratio λ of the resonant current to the grid current as

$$\lambda = \frac{I_{MF}}{I_g}. \tag{12}$$

Then, according to (8), the maximum of resonant capacitor is

$$C_{ri} \leq \frac{P_i}{3\omega U_g^2}\tan\left[\arcsin\frac{\lambda U_{\mathrm{MF}}}{2U_g\sin\frac{\theta_i+\gamma_i-\gamma_1}{2}} - \frac{\theta_i-\gamma_i-\gamma_1}{2}\right]. \tag{13}$$

The inductor is inversely proportional to resonant frequency f_r, which means a higher resonant frequency results in a small size inductor. However, the control bandwidth limits the resonant frequency. It should be noted that the selection of this resonant frequency should depend on the specific operating conditions. This article suggests that the resonant frequency is selected between the 3rd and 11th line-frequencies. It is When the resonant frequency is determined, the resonance inductor is calculated as

$$L_r \geq \frac{1}{4\pi C_r f_r^2}. \tag{14}$$

2) Number of Submodules Design: The CHB modules provide not only line-frequency voltage but also medium-frequency voltage. The number of submodules of shunt CHB can be

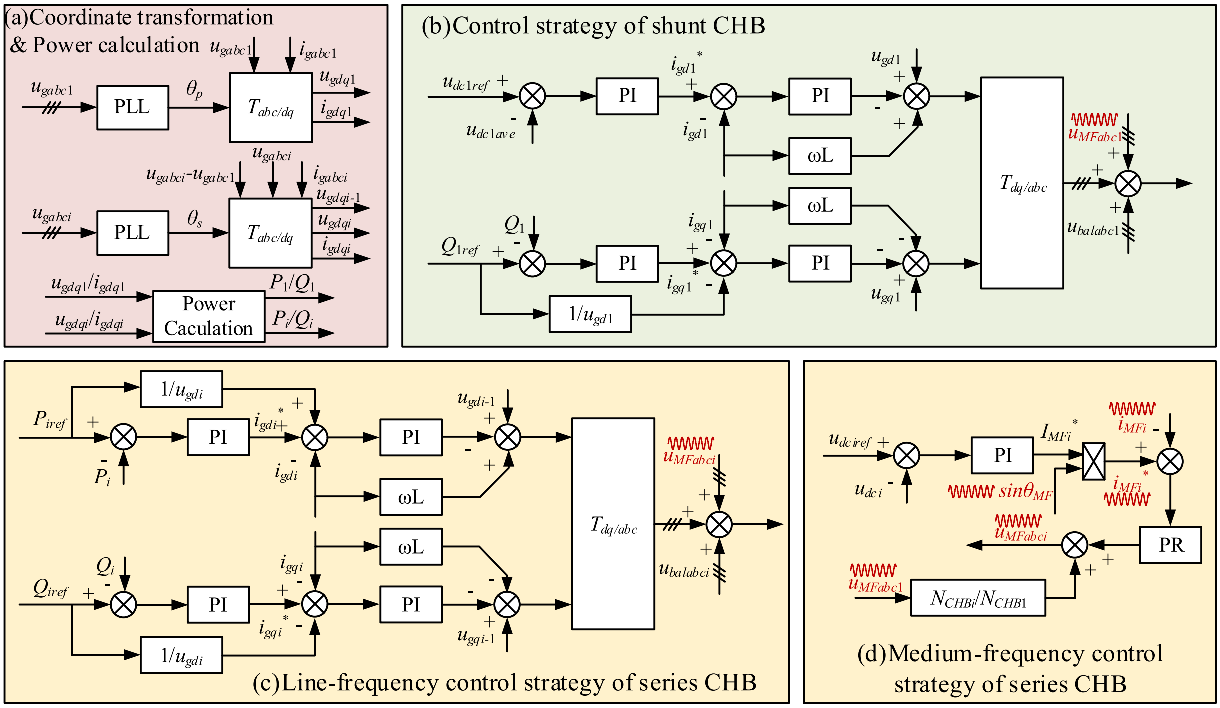

Fig. 14. Control strategy of MFSOP.

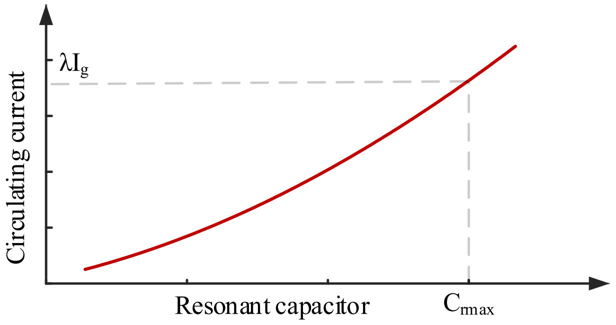

Fig. 15. Relationship between resonant capacitor and circulating current.

obtained as

$$N_1 \geq \sqrt{2}\left(\frac{U_g}{mU_{dc}} + \frac{U_{MF}}{U_{dc}}\right) \tag{15}$$

where the U_{dc} is submodule dc voltage and m is modulation index. For the second item of (15), the mixing frequency voltage u_{MF} is constant. It will not overvoltage or overshoot. Therefore, we delete the modulation index m in the denominator of second item.

When design the number of series CHB module, it is important to ensure that the series CHB can provide sufficient line-frequency and medium-frequency voltages, while at the same time ensuring that the MFSOP have the ability to withstand the fault voltage in case of a grid fault. In case of grid fault, we consider that the voltage of one of the feeder drops to zero and the series CHB is subject to the grid voltage. Therefore, the number of series CHB module is derived as

$$N_i = \sqrt{2}\max\left\{\frac{2U_g \sin\frac{\theta_{\max i}}{2}}{mU_{dc}} + \frac{U_{MF}}{U_{dc}}, \frac{U_g}{mU_{dc}}\right\} \tag{16}$$

where the $\theta_{\max i}$ is the maximum phase shift of the two feeders.

3) Submodule Capacitor Design: The minimum value of the module capacitor is designed according to the maximum fluctuation voltage of the submodule capacitor. The energy stored in all the module capacitors of the series CHB can be expressed as

$$E_{si} = \frac{1}{2}N_i C_{dcs} U_{dc}^2. \tag{17}$$

The terminal current of series CHB charges and discharges the submodule capacitor, resulting in a periodic fluctuation of the submodule capacitor voltage. The maximum and minimum values of the voltage fluctuation can be obtained as

$$\begin{cases} U_{dc,\max} = U_{dc}\,(1+\varepsilon) \\ U_{dc,\min} = U_{dc}\,(1-\varepsilon) \end{cases} \tag{18}$$

where ε is the fluctuation rate of submodule capacitor voltage, which is defined as

$$\varepsilon = \frac{U_{dc,\max} - U_{dc,\min}}{2U_{dcave}}. \tag{19}$$

Substituting (18) and (19) into (17) yields

$$\begin{aligned} \Delta E_{si} &= \frac{1}{2}N_i C_{dcs} U_{dc,\max}^2 - \frac{1}{2}N_i C_{dcs} U_{dc,\min}^2 \\ &= 2\varepsilon N_i C_{dcs} U_{dc}^2. \end{aligned} \tag{20}$$

The charging energy $\triangle E$ of the dc submodule capacitor can be calculated as

$$\Delta E = \int u_{\mathrm{CHB}i} \times i_{\mathrm{CHB}i} dt. \tag{21}$$

It is worth noted that both $u_{\mathrm{CHB}i}$ and $i_{\mathrm{CHB}i}$ consist of line-frequency components (u_{CHB1} and i_{CHB1}) and medium-frequency components ($u_{\mathrm{CHB}r}$ and $i_{\mathrm{CHB}r}$). i.e.,

$$\begin{aligned}\Delta E &= \int \left(u_{\mathrm{CHB1}} + u_{\mathrm{CHB}r}\right) \times \left(i_{\mathrm{CHB1}} + i_{\mathrm{CHB}r}\right) dt \\ &= \int u_{\mathrm{CHB1}} \times i_{\mathrm{CHB1}} dt + \int u_{\mathrm{CHB1}} \times i_{\mathrm{CHB}r} dt + \int u_{\mathrm{CHB}r} \\ &\quad \times i_{\mathrm{CHB1}} dt + \int u_{\mathrm{CHB}r} \times i_{\mathrm{CHB}r} dt \\ &= \Delta E_{1-1} + \Delta E_{1-r} + \Delta E_{r-1} + \Delta E_{r-r}.\end{aligned} \tag{22}$$

According to (1)–(4), the charging energy $\triangle E_{s1\text{-}1}$ of the line-frequency voltage and current on the submodule capacitor can be calculated as

$$\Delta E_{s1-1} = \int u_{\mathrm{CHB}i} \times i_{\mathrm{CHBi}} dt. \tag{23}$$

Therefore, the maximum fluctuation energy $\triangle E_{s1\text{-}1,\max}$ is calculated as

$$\Delta E_{s1-1,\max} = \frac{U_g I_g}{\omega} \sin\frac{\theta_i + \gamma_i - \gamma_1}{2}. \tag{24}$$

Similarly, the maximum fluctuation energy of line-frequency voltage and medium-frequency current $\triangle E_{s1\text{-}r,\max}$, medium-frequency voltage and line-frequency current $\triangle E_{sr\text{-}1,\max}$, medium-frequency voltage and medium-frequency current $\triangle E_{sr\text{-}r,\max}$ are

$$\begin{aligned}\Delta E_{s1-r,\max} &= \frac{4U_g I_{\mathrm{MF}} \omega_r}{\omega_r^2 - \omega^2} \sin\frac{\theta_i + \gamma_i - \gamma_1}{2} \\ \Delta E_{sr-1,\max} &= \frac{2U_{\mathrm{MF}} I_g \omega_r}{\omega_r^2 - \omega^2} \\ \Delta E_{sr-r,\max} &= \frac{I_{\mathrm{MF}} U_{\mathrm{MF}}}{2\omega_r}.\end{aligned} \tag{25}$$

Therefore, according to (20), (24), and (25), the capacitor of series CHB is calculated as

$$C_{\mathrm{dcs}} \geq \frac{\Delta E_{s1-1,\max} + \Delta E_{s1-r,\max} + \Delta E_{sr-1,\max} + \Delta E_{sr-r,\max}}{2\varepsilon N_i U_{\mathrm{dc}}^2}. \tag{26}$$

Similarly, for the shunt CHB, the module capacitor is designed as

$$C_{\mathrm{dcp}} \geq \frac{\Delta E_{p1-1,\max} + \Delta E_{p1-r,\max} + \Delta E_{pr-1,\max} + \Delta E_{pr-r,\max}}{2\varepsilon N_1 U_{\mathrm{dc}}^2} \tag{27}$$

where

$$\begin{aligned}\Delta E_{p1-1,\max} &= \frac{2U_g I_g}{\omega} \sin\frac{\theta + \beta}{2} \\ \Delta E_{p1-r,\max} &= \frac{4U_g \omega_r \sum I_{cir}}{\omega_r^2 - \omega^2} \\ \Delta E_{pr-1,\max} &= \frac{4U_{MF} I_g \omega_r}{\omega_r^2 - \omega^2} \sin\frac{\theta + \beta}{2} \\ \Delta E_{pr-r,\max} &= \frac{U_{MF} \sum I_{cir}}{\omega_r}.\end{aligned} \tag{28}$$

TABLE III
MFSOP TOPOLOGY PARAMETERS

Parameter	Value
Voltage of feeder#1	10∠0° kV
Voltage of feeder#2	10∠10° kV
Voltage of feeder#3	10∠−5° kV
Rated power	3 MW
Voltage of submodule capacitor	750 V
Medium-frequency voltage	1.2 kV
Number of shunt modules	16/phase
Number of series modules	13/phase
Filter inductor	4 mH
Submodule capacitor of Series CHB	1.4 mF
Submodule capacitor of shunt CHB	1.6 mF
Resonant inductor	10 mH
Resonant capacitor	10 μF

B. Design Example

With the above analysis and design procedure, a design example is presented to make an intuitive understanding of the proposed design method.

Taking a three-terminal 10 kV/3 MW MFSOP as an example, it is considered that the maximum phase shift between the two feeders is 10°. The filter inductor is 4 mH. The submodule dc voltage is 750 V. The medium-frequency voltage amplitude is selected as $20\% U_g$, i.e., $U_{\mathrm{MF}} = 1200$ V. The square wave is chosen as medium-frequency modulation wave for a smaller circulating current.

The resonance frequency is selected as 500 Hz, and the ratio in (12) is designed as $\lambda = 20\%$. According to (13) and (14), it is obtained that resonance capacitor $C_r \leqslant 12.1$ μF and the resonance inductor $L_r \geqslant 8.3$ mH. Therefore, $C_r = 10$ μF and $L_r = 10$ mH are selected.

Taking modulation index $m = 0.85$, according to (15) and (16), the number of submodules is calculated as $\mathrm{N}_{\mathrm{CHB1}} = 16$ and $\mathrm{N}_{\mathrm{CHB2}} = 13$.

According to (26) and (27), taking fluctuation rate of submodule capacitor voltage $\varepsilon = 5\%$, the series CHB submodule capacitor $C_{\mathrm{dc}s} \geqslant 1.4$ mF and the shunt CHB submodule capacitor $C_{\mathrm{dc}p} \geqslant 1.6$ mF. Thus, $C_{\mathrm{dc}s}$ and $C_{\mathrm{dc}p}$ are selected as 1.4 mF and 1.6 mF. The parameters are listed in Table III.

The MFSOP is simulated according to the above parameters, and the simulation results show that the circulating current $I_{\mathrm{MF}}/I_g = 17\%$. The submodule voltage fluctuation rate $\varepsilon_{\mathrm{s}} = 4.9\%$ for series CHB, and the submodule voltage fluctuation rate $\varepsilon_{\mathrm{p}} = 4.7\%$ for shunt CHB, which meets the design requirements.

C. Comparison of MFSOP and Traditional SOP

Taking a three-terminal 10 kV/3 MV MFSOP as an example. The phase difference of each feeder is within 10°. Table IV compares the MFSOP to other SOP topologies in terms of the number of IGBTs, the number of inductors, the number

TABLE IV
COMPARISON OF MFSOP TO OTHER SOP TOPOLOGIES

Parameter	BTB-MMC	PET	S^2-SOP	SMSOP (2 terminal)	MFSOP
Number of IGBT	936	936	180	324	504
Number of cap.	468	117	42	57	126
Number of ind.	18	9	12	6	15
Number of HFT	0	39	0	12	0
Number of port	3	3	3	2	3
Power flow regulation	decoupling	decoupling	decoupling	decoupling	decoupling
Dc port	√	×	×	×	×
Fault current isolation capability	√	√	×	√	√
Operation range	Multi-voltage level	Multi-voltage level	Same-voltage-level, small phase shift	Same-voltage-level, large phase shift	Same-voltage-level, large phase shift

TABLE V
OPERATING CONDITION OF MFSOP

Case	Time	P_1	Q_1	P_2	Q_2	P_3	Q_3
Case 1	0.2–0.4	1	0	−3	0	2	0
Case 2	0.4–0.6	3	0	−1.5	0	−1.5	0
Case 3	0.6–0.8	3	−1	−1.5	−0.5	−1.5	0.75

*The unit of active power is MW and reactive power is MVar.

of capacitors, the number of high-frequency transformers, and other features.

As can be seen from Table IV, the MFSOP saves 46% of the number of IGBTs, and does not require high-frequency transformers compared to the conventional SOP. The MFSOP have large operation range comparing to S^2-SOP and more compact in size comparing to BTB-MMC and PET.

VII. SIMULATION AND EXPERIMENTAL VERIFICATION

In order to verify the correctness of the proposed MFSOP topology and its control strategy, a simulation model and scaled-down experiment platforms are built in this section.

A. Simulation Validation

A 10 kV/3 MW three-terminal MFSOP topology is built in MATLAB/SIMULINK. The system parameters are shown in Table III.

To verify the power flow regulation capability of the MFSOP, three cases are studied, as shown in Table V.

Case 1 *(0.2–0.4 s): Unity power factor operation*

Figs. 16 –18 show the grid current, submodule dc voltage, and active/reactive power of MFSOP. During 0.2–0.4 s, the active power of three feeders is 1 MW, −3 MW, and 2 MW, respectively, and the reactive power of three feeders is zero, which means the MFSOP operates in unity power factor mode. The submodule dc voltage is 750 V, and the peak-to-peak value less than 10%. The FFT analysis shows that the total harmonic distortion of i_{g1}, i_{g2} and i_{g3} are 1.9%, 1.1%, and 1.6%, respectively. The mixed-frequency current of the *LC* branches, which includes line-frequency current and medium-frequency circulating current, as shown in Fig. 19.

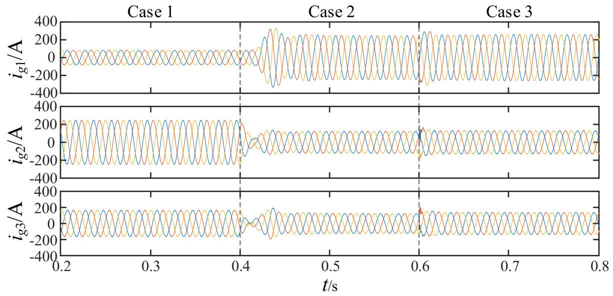

Fig. 16. Grid current of the three feeders.

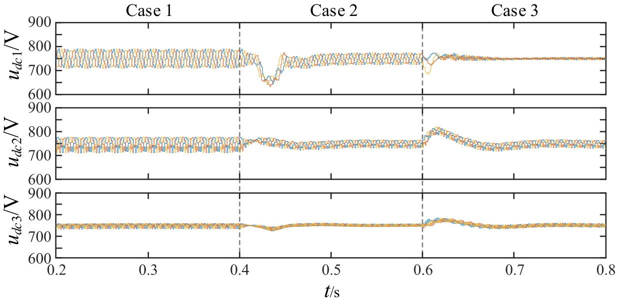

Fig. 17. Submodule DC voltage of the shunt CHB (top) and the two series CHB (middle and bottom).

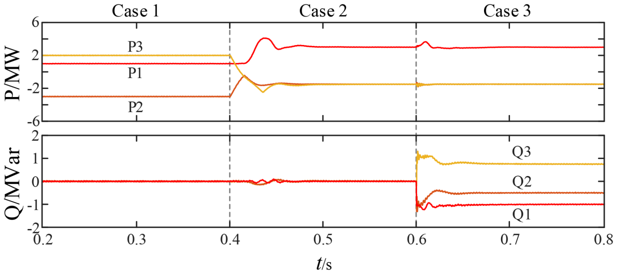

Fig. 18. Active and reactive power of the three feeders.

Case 2 (0.4–0.6 s): Active power changes

At 0.4 s, the active power of the three feeders change from 1 MW, −3 MW, and 2 MW to 3 MW, −1.5 MW, and −1.5 MW, respectively, which means that the power of feeders#1 is increased, the power of feeder#2 is halved and the power of feeder#3 is reversed, as shown in Fig. 18. As shown in Fig. 16, the current response of feeder#2 and feeder#3 is faster than that of feeder#1, that is because the feeder#1 is selected as a slack feeder. The dc voltage, as shown in Fig. 17, drops slightly but recover to set point immediately. The circulating current decrease in Fig. 19 due to the power decrease.

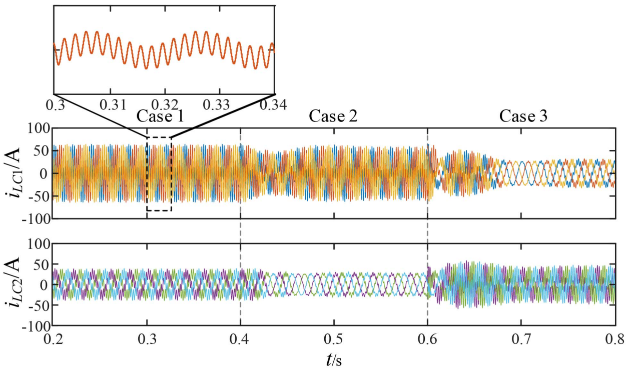

Fig. 19. Mixed-frequency current of *LC* branches.

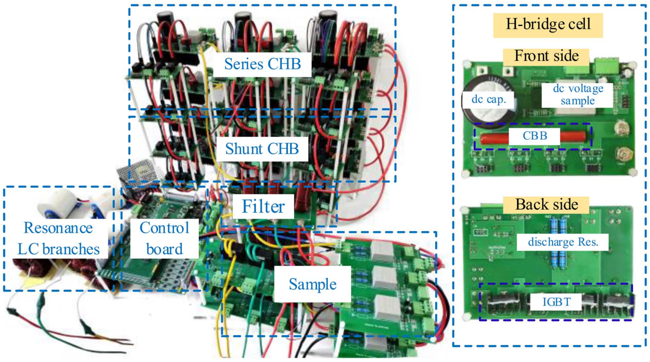

Fig. 20. Experimental prototype.

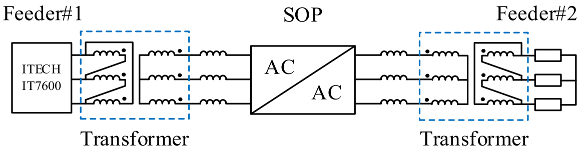

Fig. 21. Schematic of the actual experimental system.

Case 3 (0.6–0.8 s): Reactive power compensation

At 0.6 s, the active power is remained while the reactive power increases from zero to −1 MVar, 0.5 MVar, and 0.75 MVar, respectively, as shown in Fig. 19. In Fig. 16, the grid currents increase slightly because of reactive power. The submodule dc voltages u_{dc2} and u_{dc3} of CHB rise slightly because the circulating current changes.

B. Experimental Validation

An experimental platform is constructed and tested to verify the effectiveness of the proposed MFSOP topology and control strategies. The experimental prototype is shown in Fig. 20 and the schematic of the actual experimental system is shown in Fig. 21. The power grid at feeder#1 is emulated by ITECH IT7600, which is a controllable ac power supply, and the rated grid voltage/frequency is 110 V/50 Hz. Three resistors are connected in Y-connection to the output stage and each one has a resistance of 18 Ω, which means the power of experimental prototype is 2 kW. Both the series CHB and shunt CHB consist of 2 H-bridge per phase and a Y-△ transformer is equipped at the terminal. The medium-frequency voltage is set to 22 V, corresponding to the 20% of U_g. The phase difference between input and output voltage is set to 10°. The system parameters are shown in Table VI.

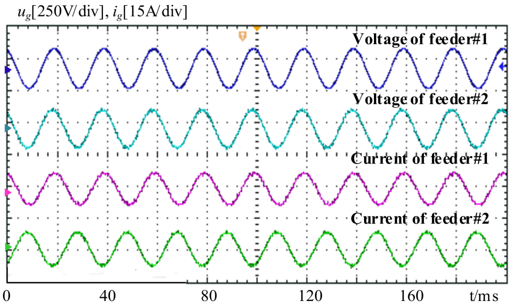

Fig. 22. Voltage and current of feeder#1 and feeder#2.

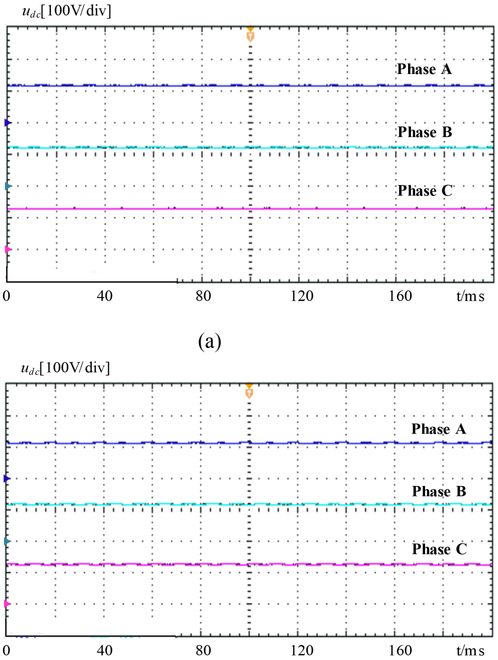

(a)

(b)

Fig. 23. Submodule voltage. (a) Submodule voltage of shunt CHB. (b) Submodule voltage of series CHB.

TABLE VI
EXPERIMENT PARAMETERS OF MFSOP

Parameters	Values	Parameters	Values
Voltage of feeder#1	110∠0° V	Voltage of feeder#2	110∠10° V
Submodule dc voltage	120 V	Medium-frequency voltage	22 V
Rated power	2 kW	Filter inductor	4 mH
Resonant inductor	10 mH	Resonant capacitor	10 μF
Submodule capacitor	1 mF	Resonant frequency	500 Hz
Number of series CHB submodule	2/phase	Number of shunt CHB submodule	2/phase

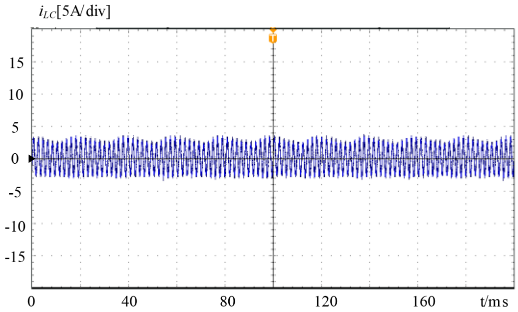

Fig. 24. Mixed-frequency current of MFSOP.

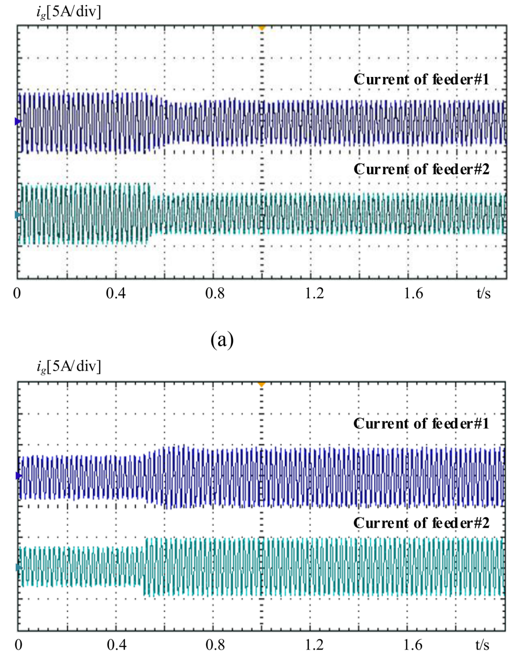

(a)

(b)

Fig. 25. Gird current during a power jump. (a) Load is decreased from 33 Ω to 50 Ω. (b) Load is increased from 50 Ω to 33 Ω.

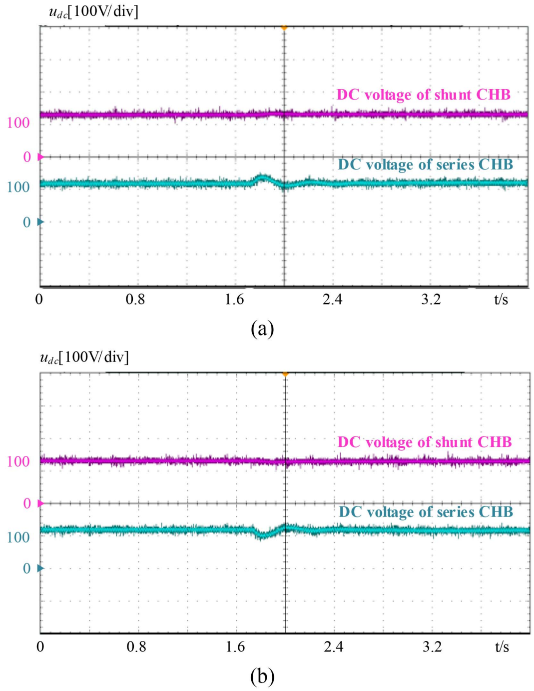

(a)

(b)

Fig. 26. DC voltage of submodule during a power jump. (a) Load is decreased from 33 Ω to 50 Ω. (b) Load is increased from 50 Ω to 33 Ω.

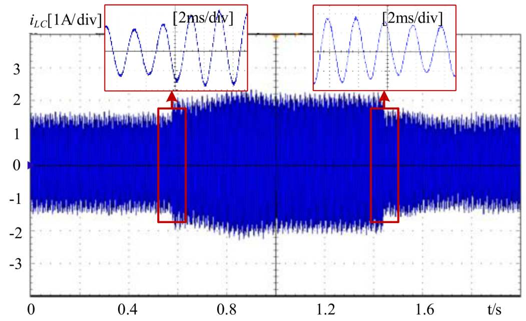

Fig. 27. Circulating current during a power jump.

Fig. 22 shows the phase-A voltage and current of feeder#1 and feeder#2. Both the voltage and current of feeder#1 and feeder#2 are in phase, which indicates that the MFSOP operates at unity power factor.

Fig. 23 shows the first submodule dc voltage of shunt CHB and series CHB. As is shown, all dc voltage is controlled to be set value 120 V and well balanced.

Fig. 24 shows the waveform of mixed-frequency current. The mixed-frequency current consists of line-frequency current and medium-frequency current. Thus, the line-frequency envelope can be seen in the waveform.

Fig. 25 shows the dynamic current waveforms of feeder#1 and feeder#2. In Fig. 25(a), the currents decrease as the load is decreased from 33 Ω to 50 Ω. The current of feeder#2 decreases immediately while the current of feeder#2 decreases slowly, which is because the feeder#2 is selected as the slack feeder. In Fig. 25(b), the currents increase as the load is increased from 50 Ω to 33 Ω. The current is stable under step change of load, which verifies the correctness of the MFSOP.

Fig. 26 shows the submodule dc voltage of series CHB and shunt CHB during the power jump (Only the voltage of phase-A is shown here). It can be seen that the dc voltage of series CHB fluctuates slightly but recovers immediately, while the voltage of the shunt CHB remains almost constant.

Fig. 27 shows the resonant current during the power jump. It can be seen that the current rises immediately when the load increased and stabilizes after a period of overshoot. Then, the current drops immediately when the load decreased.

Fig. 28 shows the active power and reactive power during a power jump. The active power jumps from 1.1 kW to 0.73 kW when the load is changed from 33 Ω to 50 Ω. The reactive power jumps from 0 Var to −600 Var and then to 300 Var. It is worth

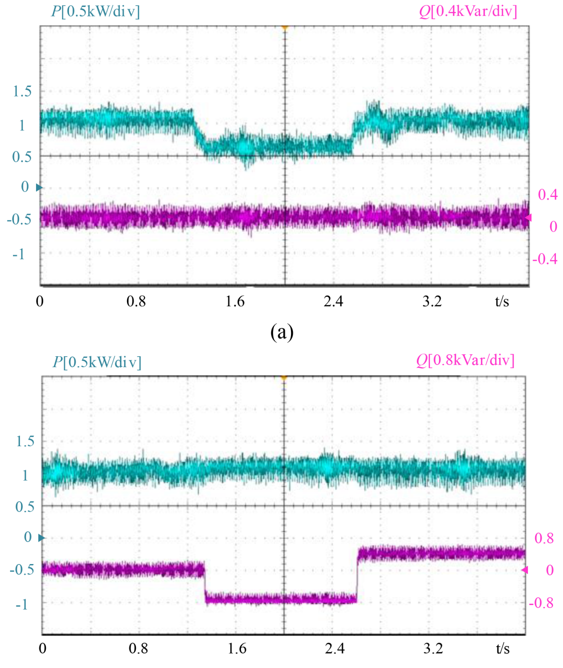

(a)

(b)

Fig. 28. Active power and reactive power during a power jump. (a) Load is increased from 50 Ω to 33 Ω and then decreased back to 50 Ω. (b) Reactive power jumps from 0 Var to −600 Var and then to 300 Var.

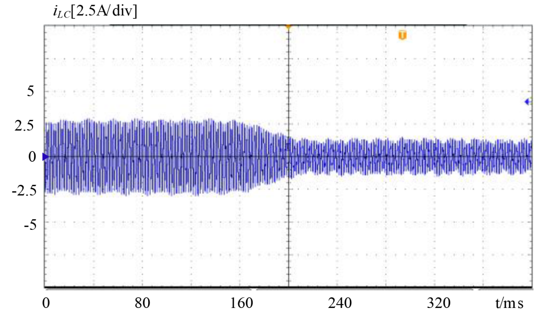

Fig. 29. Circulating current during a reactive power changed.

noting that the active power and reactive power are calculated by the DSP and output from the DAC.

In Fig. 29, the circulating current is shown when the reactive power changed from 0 Var to 200 Var. It can be seen that the circulating current decreases, which verifies the correctness of the proposed suppression method of circulating current.

Fig. 30(a) shows the experimental and theoretical results of circulating current when the phase shift changed. The phase shift is set as 10°, 15°, and 20°. Fig. 30(b) shows the circulating current when the reactive power is −100 Var, −150 Var, and −200 Var. It is worth noting that inductor of transformer should be considered in here. The inductor of transformer is 5.3 mH. The active power is 2 kW. And the circulating current i_{LC} consists of medium frequency current i_{MF} and line-frequency current i_1. It can be seen that the experimental results almost coincide with the theoretical results, which verifies the correctness of the circulating current models and suppression method.

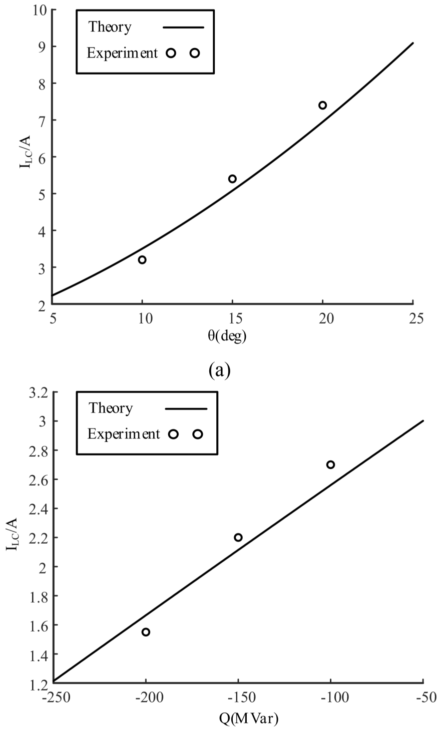

(a)

(b)

Fig. 30. Experimental and theoretical results of the circulating current. (a) Different phase shift. (b) Different reactive power.

VIII. Conclusion

A new mixed-frequency modulation based soft open point is proposed in this article. Compared with the traditional BTB-MMC, the proposed MFSOP reduces the number of submodules, which makes the SOP more compact in size. The control strategies are described and the circulating current model are analyzed. The mixed-frequency modulation strategy introduces a medium-frequency circulating current in the MFSOP, which increases the current stress. Therefore, two circulating current suppression strategies are proposed. The first strategy is to suppress the circulating current by reducing a little bit of power factor, and the second strategy is to suppress circulating current by replacing the sinusoidal medium-frequency modulation waveform with a square wave. Both strategies can be adopted at the same time. Some key parameters, including resonance *LC*, submodule capacitor and number of submodule, are designed and the comparison of the MFSOP and other SOP topologies is listed. From the list, it can be concluded that the MFSOP can save submodules compared with the BTB-MMC and PET, which reduces the cost and improve the efficiency.

References

[1] X. Jiang, Y. Zhou, W. Ming, P. Yang, and J. Wu, "An overview of soft open points in electricity distribution networks," *IEEE Trans. Smart Grid*, vol. 13, no. 3, pp. 1899–1910, May 2022.

[2] T. Asakura, T. Genji, T. Yura, N. Hayashi, and Y. Fukuyama, "Long-term distribution network expansion planning by network reconfiguration and generation of construction plans," *IEEE Trans. Power Syst.*, vol. 18, no. 3, pp. 1196–1204, Aug. 2003.

[3] W. Cao et al., "Operating principle of soft open points for electrical distribution network operation," *Appl. Energy*, vol. 164, pp. 245–257, 2016.

[4] K. S. Fuad, H. Hafezi, K. Kauhaniemi, and H. Laaksonen, "Soft open point in distribution networks," *IEEE Access*, vol. 8, pp. 210550–210565, 2020.

[5] T.-T. Ku, C.-H. Lin, C.-S. Chen, and C.-T. Hsu, "Coordination of transformer on-load tap changer and PV smart inverters for voltage control of distribution feeders," *IEEE Trans. Ind. Appl.*, vol. 55, no. 1, pp. 256–264, Jan./Feb. 2019.

[6] C. Long and L. F. Ochoa, "Voltage control of PV-Rich LV networks: OLTC-fitted transformer and capacitor banks," *IEEE Trans. Power Syst.*, vol. 31, no. 5, pp. 4016–4025, Sep. 2016.

[7] J. M. Bloemink and T. C. Green, "Increasing distributed generation penetration using soft normally-open points," in *Proc. IEEE PES Gen. Meeting*, 2010, pp. 1–8.

[8] J. M. Bloemink and T. C. Green, "Increasing photovoltaic penetration with local energy storage and soft normally-open points," in *Proc. IEEE Power Energy Soc. Gen. Meeting*, 2011, pp. 1–8.

[9] X. Liang, M. A. Saaklayen, M. A. Igder, S. M. R. H. Shawon, S. O. Faried, and M. Janbakhsh, "Planning and service restoration through microgrid formation and soft open points for distribution network modernization: A review," *IEEE Trans. Ind. Appl.*, vol. 58, no. 2, pp. 1843–1857, Mar./Apr. 2022.

[10] Y. Qi, Y. Li, W. Li, H. Deng, and Y. Tang, "Autonomous control of soft open point for distribution network reliability enhancement," *IEEE J. Emerg. Sel. Topics Power Electron.*, vol. 11, no. 3, pp. 3127–3137, Jun. 2023.

[11] Z. Ma, J. Chen, Z. Fang, Y. Hao, and G. Yang, "A seamless transfer control strategy of SNOP for the critical load safety under network faults," in *Proc. IEEE 9th Int. Power Electron. Motion Control Conf.*, 2020, pp. 2347–2351.

[12] B. Han, S. Baek, H. Kim, and G. Karady, "Dynamic characteristic analysis of SSSC based on multibridge inverter," *IEEE Trans. Power Del.*, vol. 17, no. 2, pp. 623–629, Apr. 2002.

[13] L. Baruschka and A. Mertens, "A new three-phase AC/AC modular multilevel converter with six branches in hexagonal configuration," *IEEE Trans. Ind. Appl.*, vol. 49, no. 3, pp. 1400–1410, May/Jun. 2013.

[14] J. Pereda and T. C. Green, "Direct modular multilevel converter with six branches for flexible distribution networks," *IEEE Trans. Power Del.*, vol. 31, no. 4, pp. 1728–1737, Aug. 2016.

[15] J. Song, Y. Zhang, Z. Gao, C. Cao, Z. Wang, and F. Xu, "Research on topology and control technology of soft multi-state open point with fault isolation capability," in *Proc. China Int. Conf. Electricity Distrib.*, 2018, pp. 1467–1473.

[16] X. Wang, J. Liu, S. Ouyang, T. Xu, F. Meng, and S. Song, "Control and experiment of an H-bridge-based three-phase three-stage modular power electronic transformer," *IEEE Trans. Power Electron.*, vol. 31, no. 3, pp. 2002–2011, Mar. 2016.

[17] S. Ouyang, J. Liu, Y. Yang, X. Chen, S. Song, and H. Wu, "DC voltage control strategy of three-terminal medium-voltage power electronic transformer-based soft normally open points," *IEEE Trans. Ind. Electron.*, vol. 67, no. 5, pp. 3684–3695, May 2020.

[18] J. Zhang et al., "Series–shunt multiport soft normally open points," *IEEE Trans. Ind. Electron.*, vol. 70, no. 11, pp. 10811–10821, Nov. 2023.

[19] H. Peng, J. Zhang, J. Zhou, G. Shi, J. Wang, and X. Cai, "Delta-type series shunt soft normally-open points with wide power flow regulation range in distributed network," *IEEE Trans. Ind. Electron.*, vol. 71, no. 7, pp. 6501–6511, Jul. 2024.

[20] H. Zhao, W. Chen, G. He, and J. Wang, "A new shared module soft open point for power distribution network," *IEEE Trans. Power Electron.*, vol. 38, no. 3, pp. 3363–3374, Mar. 2023.

[21] Z. Yuan, S. W. H. de Haan, J. B. Ferreira, and D. Cvoric, "A FACTS device: Distributed power-flow controller (DPFC)," *IEEE Trans. Power Electron.*, vol. 25, no. 10, pp. 2564–2572, Oct. 2010.

[22] J. Lan, W. Chen, X. Li, Y. Sun, L. Shu, and F. Deng, "A three-phase multiplexing arm modular multilevel converter with high power density and small volume," *IEEE Trans. Power Electron.*, vol. 37, no. 12, pp. 14587–14600, Dec. 2022.

[23] J. Lan, W. Chen, X. He, Y. Xie, and Y. Wang, "The wide multiplexed period three-phase multiplexing arm modular multilevel converter," *IEEE J. Emerg. Sel. Topics Power Electron.*, vol. 11, no. 5, pp. 4929–4944, Oct. 2023.

[24] Y. Xue, Z. Xu, and Q. Tu, "Modulation and control for a new hybrid cascaded multilevel converter with DC blocking capability," *IEEE Trans. Power Del.*, vol. 27, no. 4, pp. 2227–2237, Oct. 2012.

[25] D. Ma, W. Chen, L. Shu, X. Qu, S. Gao, and K. Hou, "A multiport AC–AC–DC converter for soft normally open point," *IEEE Trans. Circuits Syst. II, Exp. Briefs*, vol. 69, no. 4, pp. 2146–2150, Apr. 2022.

[26] K. Hu et al., "A linear and simplified cluster voltage balancing control based on the zero-sequence voltage injection for star-connected cascaded H-bridge STATCOM," *CSEE J. Power Energy Syst.*, vol. 10, no. 5, pp. 2255–2264, Sep. 2024.

[27] H. Akagi, S. Inoue, and T. Yoshii, "Control and performance of a transformerless cascade PWM STATCOM with star configuration," *IEEE Trans. Ind. Appl.*, vol. 43, no. 4, pp. 1041–1049, Jul./Aug. 2007.